

# Realization of omnidirectional ultra-broadband antireflection properties via subwavelength composite structures

Likai Zheng<sup>1</sup> · Yimin Xuan<sup>1</sup>

Received: 10 July 2017 / Accepted: 3 October 2017 / Published online: 13 October 2017  
© Springer-Verlag GmbH Germany 2017

**Abstract** An advanced subwavelength composite structure (SCS) consisting of the hexagonally arranged silicon nanopillars and the misaligned TiO<sub>2</sub>/SiO<sub>2</sub> double-layer films was proposed on the surface of crystalline silicon (c-Si). After optimization through the finite difference time domain (FDTD) method, the SCS possesses omnidirectional ultra-broadband antireflection properties (average reflectance < 1.8% within 300–2500 nm) which are suitable for a photovoltaic-thermoelectric (PV-TE) hybrid system to enhance the full-spectrum solar energy utilization. Furthermore, the antireflection mechanism was studied in detail. The composition of nanopillars and double-layer films has combined the effect of interference, interpillar scattering and waveguide resonance to realize outstanding antireflection properties. The SCS was prepared on a 3 cm × 3 cm silicon wafer by ICP etching and magnetron sputtering, and the measured results matched well with the simulation results. Further, such antireflection concept can be applied to other materials for particular ultra-broadband spectrum regulation.

## 1 Introduction

With the gradually increasing energy consumption and the approaching exhaustion of traditional fossil fuel, finding new forms of energy sources has become one of the most urgent missions for the human beings. Being a sort of clean, inexhaustible and inexpensive energy, solar energy is considered

as a promising renewable energy for solving the energy crisis. As one of the most efficient ways to utilize solar energy, crystalline silicon (c-Si) solar cells have received extensive attention due to their low cost in raw materials and high performance in photoelectric conversion [1, 2]. For planar silicon photovoltaic (PV) cells, over 30% of incident energy will be reflected on the interface of silicon and air because of the refractive index difference between these two optical mediums [3], resulting in significantly decreased photoelectric conversion efficiency of PV cells. Therefore, a variety of methods of light trapping mechanisms on PV cells were proposed to reduce the reflection of incident light, including antireflection coatings (ARCs) [4–16], and textured nanostructure surfaces [17–24].

Due to the limit of Si band gap, few researchers were concerned about the capture of light at wavelengths greater than 1100 nm. However, the solar radiation energy is mainly distributed at wavelengths between 300 and 2500 nm according to the AM1.5 solar spectrum [25], which means a considerable part of the solar energy is wasted without any utilization by silicon PV cells. In order to improve the utilization efficiency of solar energy, the photovoltaic-thermoelectric (PV-TE) hybrid system was proposed [26, 27], which is capable to utilize the full spectrum solar energy by coupling a TE device on the back side of a c-Si PV cell to absorb and convert the waste heat into electric energy. Thus, an efficient antireflection surface aiming for full spectrum (300–2500 nm) should be obtained on the top of the PV-TE hybrid system (as shown in Fig. 1). Besides, since the incident angle of sunlight varies over time during the day, a structure that possesses omnidirectional antireflection properties is necessary.

Recently, several researches indicated that structures possessing graded refractive indexes profile have great potentials on full spectrum and wide angle antireflection

✉ Yimin Xuan  
ymxuan@nuaa.edu.cn

<sup>1</sup> College of Energy and Power Engineering, Nanjing University of Aeronautics and Astronautics, Nanjing 210016, China

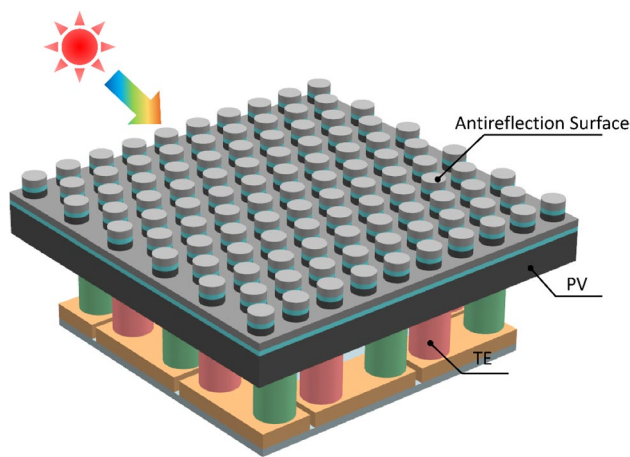


**Fig. 1** Schematic of the PV-TE system. The antireflection surface of the PV cells is designed for full spectrum (300–2500 nm) light capture. Some of the solar energy is utilized by the PV cells, and the unused energy would be utilized by the TE devices which are coupled on the back side of the PV cells

[28–31]. For further application of these properties to reality, it is necessary to develop a structure that is convenient and controllable in fabrication. As two methods of photon management, nanopyllars and thin-film ARCs have remarkable capabilities in spectrum tuning [13, 32], whose morphologies are controllable and convenient in fabrication. This indicates that a composite structure possessing gradient refractive indexes profile which is composed of nanopyllars and thin-film ARCs may be a suitable candidate. A research paper by Spinelli et al. [33] has shown that the combination of Si nanopyllars and a Si<sub>3</sub>N<sub>4</sub> ARC can provide excellent antireflection property on Si surface. However, in that work, researchers only considered about the antireflection for wavelengths at 400–900 nm, and the antireflection mechanism of the composition of nanopyllars and ARC has only been simply discussed.

In this paper, a subwavelength composite structure (SCS) is proposed on the front surface of silicon solar cells for a PV-TE hybrid system to enhance the solar energy utilization. The SCS combines a textured structure of hexagonal nanopyllars array with the TiO<sub>2</sub>/SiO<sub>2</sub> double-layer ARCs, and possesses ultra-broadband antireflection properties for wide angles of incidence according to the simulation results, which are then confirmed by the experimental results. We found that the outstanding antireflection proprieties of the SCS are not only respectively due to the interference effect of the double-layer films and the scattering effect of the nanopyllars, but also due to the gradient refractive indexes in the air/Si interface and the waveguide resonances stimulated by nanopyllars and surrounding materials, which are caused by the composition of nanopyllars and double-layer films. Further, this antireflection concept can applied to other materials for particular ultra-broadband spectrum regulation.

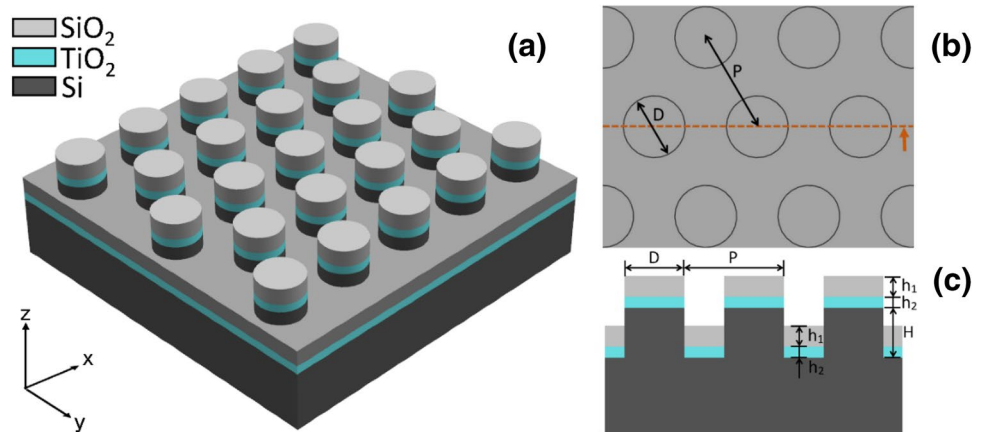
## 2 Simulation method

### 2.1 Simulation model

A basic schematic of the SCS on the top surface of the PV cell is shown in Fig. 2(a). It consists of the periodic hexagonal array of silicon nanopyllars formed on a c-Si substrate and the misaligned stacked double-layer antireflection coatings coated on both the top of the nanopyllars and the substrate surface. Acting as the intermediate index optical medium between air and silicon, the double-layer ARCs is used for reducing the reflectance of the visible light that carries significant amount of solar energy according to the AM1.5 solar irradiation spectrum. In order to obtain a minimum reflectance at the adjacent range of the design wavelength  $\lambda_0$ , the requisite index condition for the double-layer ARCs with equal optical thickness ( $n_1h_1 = n_2h_2 = \lambda_0/4$ ) is [34]:

$$\begin{cases} n_1^3 = n_0^2 \cdot n_s^2 \\ n_2^3 = n_0 \cdot n_s^3 \end{cases} \quad (1)$$

**Fig. 2** a Schematic of the SCS. b Top view of the structure. c Structure profile along the dashed line



where  $n_0$  is the refraction index of air, and  $n_s$  is the refraction index of the substrate.  $n_1$  and  $n_2$  are refraction indexes of the top layer and the bottom layer, respectively.  $h_1$  and  $h_2$  are the thicknesses of the top layer and the bottom layer, respectively.

Since the substrate of the PV cell is crystalline silicon, whose refractive index  $n_s$  is nearly 3.93 at the wavelength of 600 nm [35], and  $n_0$  (air) = 1, the required refractive indexes, determined by Eq. (1), are  $n_1 = 1.58$  and  $n_2 = 2.49$  at the design wavelength of 600 nm, respectively. Thus, SiO<sub>2</sub> and TiO<sub>2</sub> are chosen as the materials of the double-layer ARCs because of their excellent optical transmittance and suitable refractive indexes [ $n_1$  (SiO<sub>2</sub>) = 1.46 and  $n_2$  (TiO<sub>2</sub>) = 2.60 at wavelength of 600 nm] [35] that are approximate to the required values. In this case, the thickness of each layer would approximately be  $h_1 = 105$  nm and  $h_2 = 55$  nm to meet the condition of equal optical thickness. Figure 2(b) gives the top view of the SCS, and Fig. 2(c) shows the structure profile along the dashed line.  $D$  and  $H$  represent the diameters and the heights of the nanopillars respectively, and  $P$  represents the pitches of the nanopillars.

### 2.2 Simulation method

The finite difference time domain (FDTD) method is used for solving a set of Maxwell’s curl equations [Eq. (2)] to simulate the propagation of incident light as well as the interactions between electromagnetic waves and the structure [30]:

$$\begin{cases} \nabla \times H = \frac{\partial D}{\partial t} \\ D = \epsilon E \\ \nabla \times E = -\frac{\partial B}{\partial t} \\ B = \mu H \end{cases} \quad (2)$$

where  $E$  is the electric field,  $H$  is the magnetic field,  $D$  is the electric displacement field,  $B$  is the magnetic flux density,  $\epsilon$  is complex permittivity, and  $\mu$  is complex permeability. Since the  $\epsilon$  is frequency-dependent, the frequency domain equation  $D(\omega) = \epsilon(\omega)E(\omega)$  should be transformed to the time domain by using the auxiliary difference equation (ADE). The central difference approximations are applied for both the temporal and spatial derivatives of Eq. (2). For ensuring the convergence of algorithm, the time step should be  $\Delta t = \delta/(2c)$ , where  $\delta$  is the smallest space step, and  $c$  is the speed of light in vacuum. For numerical calculation, the structured grid is used for discretization of the simulation region, and corresponding electromagnetic parameters determined by initial and boundary conditions are assigned to each grid.

Figure 3 shows a period unit cell of the SCS with a dashed frame representing the simulation region. Considering the SCS is periodic in the  $x$ - and  $y$ - directions, the periodic boundary conditions are applied in the  $x$ - and  $y$ - directions. In addition, assuming that photons trapped by the SCS are completely absorbed by the PV-TE hybrid system, the perfect match layer (PML) boundary conditions [36] are applied in the  $z$ - direction to set an infinite thickness substrate. Moreover, the direction of solar radiation is determined by the polar angle ( $\theta$ ) and the azimuthal angle ( $\varphi$ ) which was supposed to be zero in this work.

## 3 Result and discussion

### 3.1 Optimization of the SCS

In order to study the effect of the nanopillars parameters on the antireflection properties of the SCS, the thicknesses of the ARCs are set as  $h_1 = 105$  nm and  $h_2 = 55$  nm. Therefore, the structure morphology of the SCS is related to the values of  $P$ ,  $D$  and  $H$  as the thicknesses of ARCs ( $h_1$  and  $h_2$ ) have been determined. Hence, with a given value of  $P$ , the structure feature can be specified by two dimensionless numbers which are  $N_1 = H/P$  and  $N_2 = D/P$ . In order to identify the optimized parameters of the SCS in antireflection, the average reflectance of a series of structures with different parameters over a broadband wavelength range of 300–2500 nm was calculated as [37]:

$$R_{ave} = \frac{\int_{300nm}^{2500nm} R_{(\lambda)} I_{(\lambda)} d\lambda}{\int_{300nm}^{2500nm} I_{(\lambda)} d\lambda} \quad (3)$$

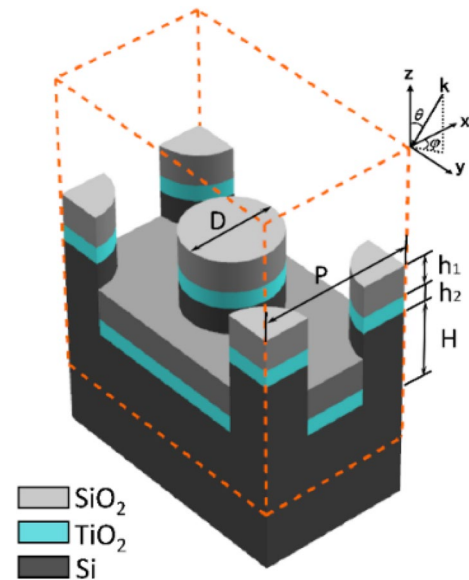


Fig. 3 Schematic of one period of the SCS

where  $R_{(\lambda)}$  is the spectral reflectance, and  $I_{(\lambda)}$  is the solar irradiance from the AM1.5.

Figure 4 shows the average reflectance of different morphologies of simulation models which are modified by changing the dimensionless numbers ( $N_1 = H/P = 0.2-0.9$  and  $N_2 = D/P = 0.4-0.7$ ) with four different value of pitches  $P$ . As can be seen from the figure, structures with the dimensionless number  $N_2$  ( $D/P$ ) of 0.6 always have the lowest average reflectance among all structures as the value of  $P$  varies from 300 to 600 nm. Furthermore, the dimensionless number  $N_1$  ( $H/P$ ) of structures with minimum reflectance shifts from 0.8 to 0.5 over different values of  $P$ , indicating that the optimal height  $H$  of nanopillars is almost maintained at about 250 nm. That is to say, those structures with minimum average reflectance have the same coverage rate and height of nanopillars even though their morphologies are different.

### 3.2 Antireflection properties and discussion

For further study, we perform the simulation of the reflectance spectrum of optimized SCSs with different  $P$  for wavelengths over 300–2500 nm along with the AM1.5 solar irradiance spectrum, as shown in Fig. 5 The reflectance of a bare flat Si surface and a flat Si substrate coated with  $\text{TiO}_2/\text{SiO}_2$  (55 nm/105 nm) double-layer ARCs are also shown for comparison. The data in Fig. 5 show that the optimized SCSs reduce the reflectance of the Si surface over the full spectral range, which obtain ultra-low average reflectance of 1.3%–1.8%, weighted with the AM1.5 solar

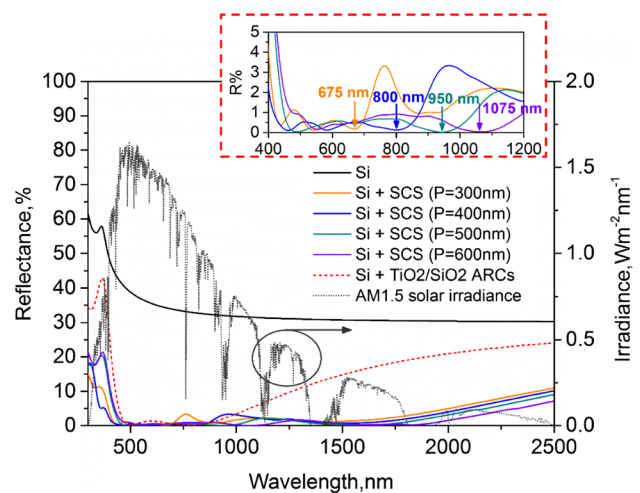
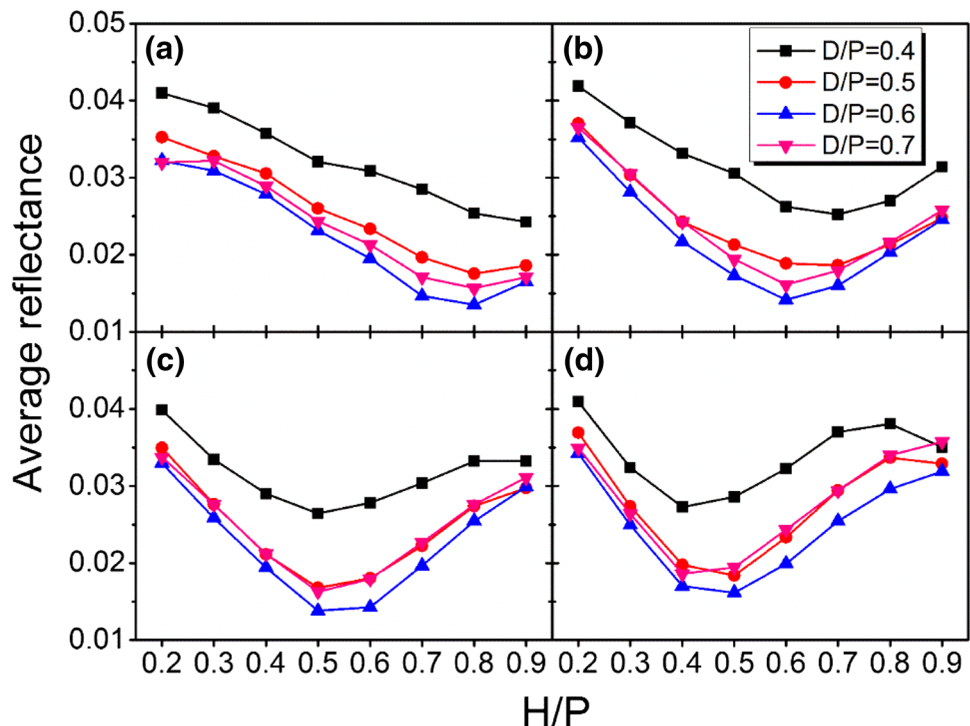


**Fig. 5** The reflectance spectrum of optimized SCSs with different  $P$  for wavelengths over 300–2500 nm along with the AM1.5 solar irradiance spectrum. The right arrow refers plotted data to the right vertical axis. The inserted picture shows the reflectance details of the SCSs for wavelengths from 400 to 1200 nm, where the zero reflectance appears at wavelength  $\lambda = 675$ ,  $\lambda = 800$ ,  $\lambda = 950$ , and  $\lambda = 1075$  nm are marked by arrows

spectrum. As can be noticed, the reflectance curves of the optimized SCSs with different  $P$  have the same tendencies and are closed to each other at wavelengths greater than 1200 nm. This is due to the similar gradient effective refractive indexes profiles as the coverage rates and heights of nanopillars of these optimized SCSs are the same. The

**Fig. 4** Average reflectance of simulation models with different parameters. **a**  $P = 300$  nm; **b**  $P = 400$  nm; **c**  $P = 500$  nm; **d**  $P = 600$  nm



inserted picture in Fig. 5 shows the reflectance details for wavelengths from 400 to 1200 nm. It can be seen that the tendencies of reflectance curves for these optimized SCSs with different  $P$  do not match well with each other for wavelengths from 650 to 1200 nm. This indicates that the antireflection properties for short wavelength region are determined by the specific morphology of the SCS instead of the general approximate profile because of the wavelength of incident light are close to the feature sizes of the SCS.

By comparing the reflectance curves of the SCSs with the double-layer ARCs, it can be seen that the reflectance of all optimized SCSs has been decreased to less than 1% around 600 nm wavelength by the designed double-layer ARCs. For further explanations, the electric (E) field distributions in the  $x$ - $z$  cross section of the structures with and without ARCs were calculated for 600 nm wavelength as shown in Fig. 6a and b, respectively. It can be found that the incident light is well captured by the SCS with the help of ARCs, while it is strongly reflected by the structure without ARCs. In addition, Fig. 6c and d illustrate the Poynting vector distributions (representing the energy density distributions) of these two structures corresponding to Fig. 6a and b. With the assistance of ARCs, most of the energy of the incident light will finally enter the nanopillars and be absorbed by the Si, while some of the energy will outflow without ARCs.

Moreover, the inserted picture in Fig. 5 shows that several zero reflectance appear at different wavelengths of 675, 800, 950 and 1075 nm with different  $P$  of 300, 400, 500 and 600 nm, respectively. For thorough investigations of this phenomenon, the E field distributions of the optimized SCSs were calculated as shown in Figs. 7 and 8. Figure 7 illustrates the E field distributions in the  $x$ - $z$  cross section of the SCSs for wavelengths where zero reflectance appears with different  $P$ . It can be found that the incident light is strongly scattered by nanopillars to adjacent ones, increasing the optical path length of light that is unabsorbed in the initial moment of interaction between incident light and the structure. As a result, large amount of the incident light is trapped and finally absorbed by the SCS instead of being reflected.

On the other hand, Fig. 8 shows the E field distribution in the  $x$ - $y$  cross section near the bottom of a single nanopillar with simulation parameters corresponding to Fig. 7. Although the diameters of these nanopillars are different, the similar E field resonances can be observed inside the nanopillars (as shown in Fig. 8a-d). In fact, the single nanopillar can act as a cylinder dielectric waveguide because of the higher refractive index in comparison to the surrounding medium, and the resonance is caused by the leaky waveguide modes, which are defined by (consider nonmagnetic materials) [38]:

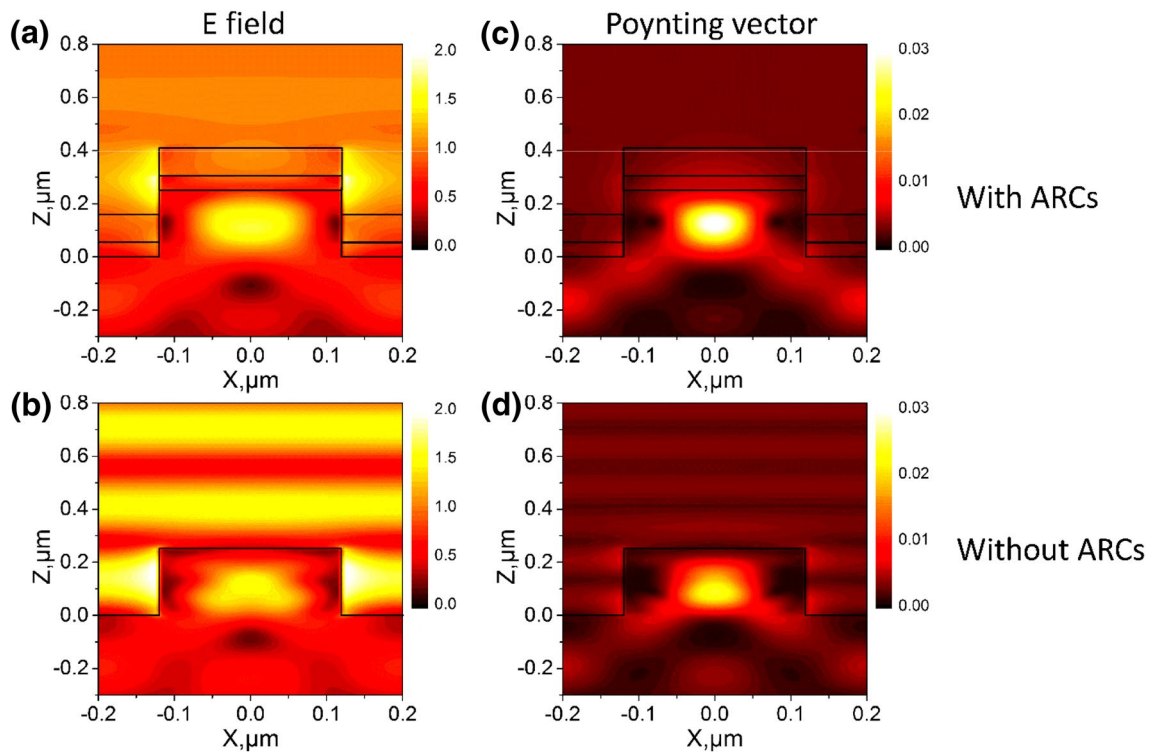


**Fig. 6** **a** E field distribution at wavelength of 600 nm in the  $x$ - $z$  cross section of the SCS with ARCs and **b** without ARCs; **c** Poynting vector distribution at wavelength of 600 nm in the  $x$ - $z$  cross section of the SCS with ARCs and **d** without ARCs

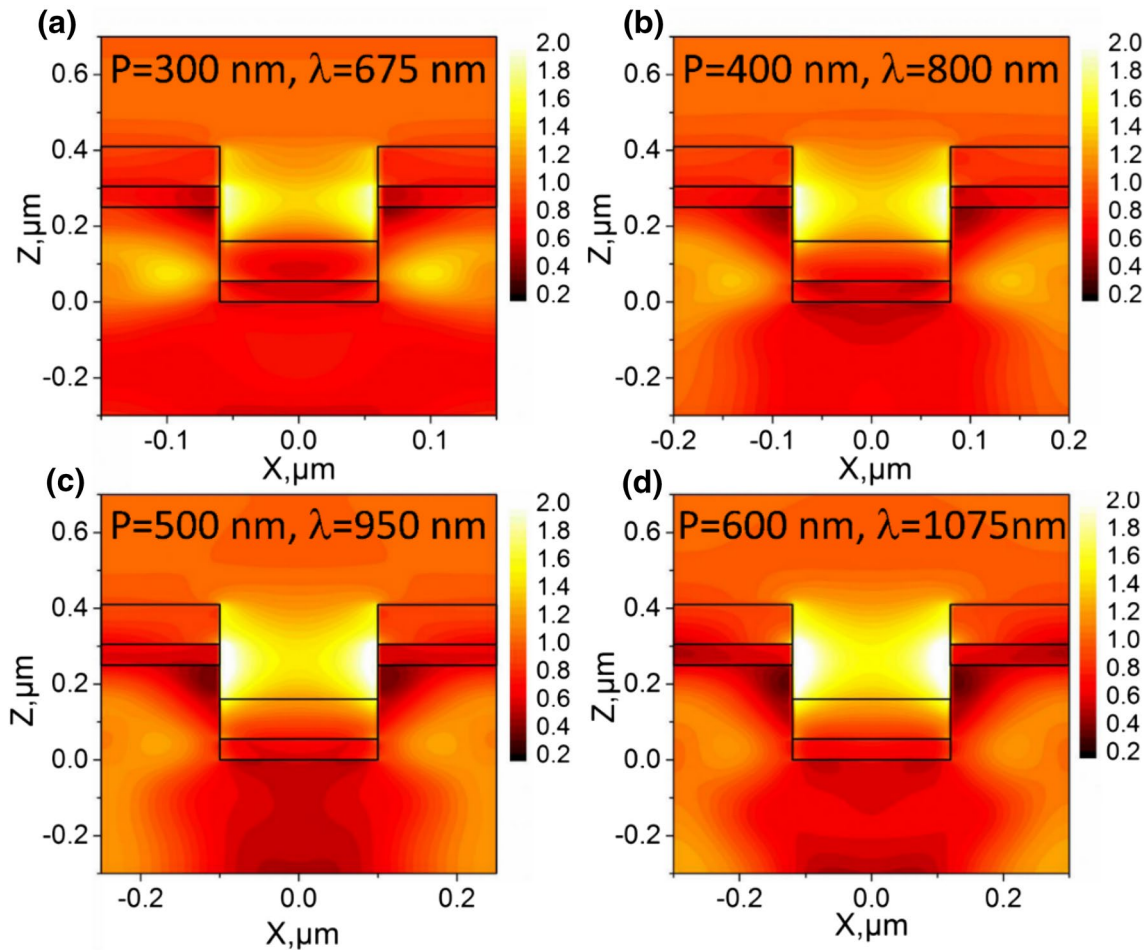


**Fig. 7** The E field distribution in the  $x$ - $z$  cross section of the SCSs for wavelengths where zero reflectance appears with different  $P$

$$\left( \frac{1}{u} \frac{J'_m(u)}{J_m(u)} - \frac{1}{v} \frac{H'_m(v)}{H_m(v)} \right) \left( \frac{\epsilon_{cyl}}{u} \frac{J'_m(u)}{J_m(u)} - \frac{\epsilon_{sur}}{v} \frac{H'_m(v)}{H_m(v)} \right) = \pm \left( \frac{1}{v^2} - \frac{1}{u^2} \right)^2 \left( \frac{k_z m}{k_0} \right)^2 \tag{4}$$

where  $m$  is the order of the cylindrical Bessel ( $J_m$ ) and first kind Hankel ( $H_m$ ) functions,  $a$  is the radius of the cylinder,  $\epsilon_{cyl}$  and  $\epsilon_{sur}$  are the dielectric permittivity of the cylinder and surrounding medium respectively,  $k_0 = 2\pi/\lambda$  is the free-space wavenumber, and

$$u = k_{cyl} \cdot r = a \cdot \sqrt{\epsilon_{cyl} \cdot k_0^2 - k_z^2} \tag{5a}$$

$$v = k_{sur} \cdot r = a \cdot \sqrt{\epsilon_{sur} \cdot k_0^2 - k_z^2} \tag{5b}$$

In this case, the material of the cylinder and surrounding medium is Si and  $\text{TiO}_2$  respectively. The radii of the nanopillars in Fig. 8a–d are, respectively, 90, 120, 150, and 180 nm of the optimized SCS with different pitches of 300, 400, 500, and 600 nm. The resonance wavelengths

with  $\text{TM}_{11}$  mode predicted by Eq. (4) are 667, 835, 1000, and 1180 nm for the geometry parameters defined in Fig. 8a–d, respectively. These values have a good agreement with the reflectance valley, locating at 675, 800, 950, and 1075 nm. Therefore, the zero reflectance is due to the combined effect of waveguide and interpillar scattering. For further studies of the SCS’s antireflection properties, the reflectance spectrum of multi-angle incident light with TM (p) and TE (s) polarization for the specific parameters (i.e.,  $H = 250$  nm,  $D = 300$  nm,  $P = 500$  nm,  $h_1 = 105$  nm and  $h_2 = 55$  nm) were calculated. Figure 9a and b give the color maps for the reflectance spectrum of the SCS with TM and TE polarized light for wavelengths of 300–2500 nm at multiple angles of incidence ( $0^\circ$ – $60^\circ$ ). The omnidirectional ultra-low reflectance can be observed for both TM and TE polarization over a wide

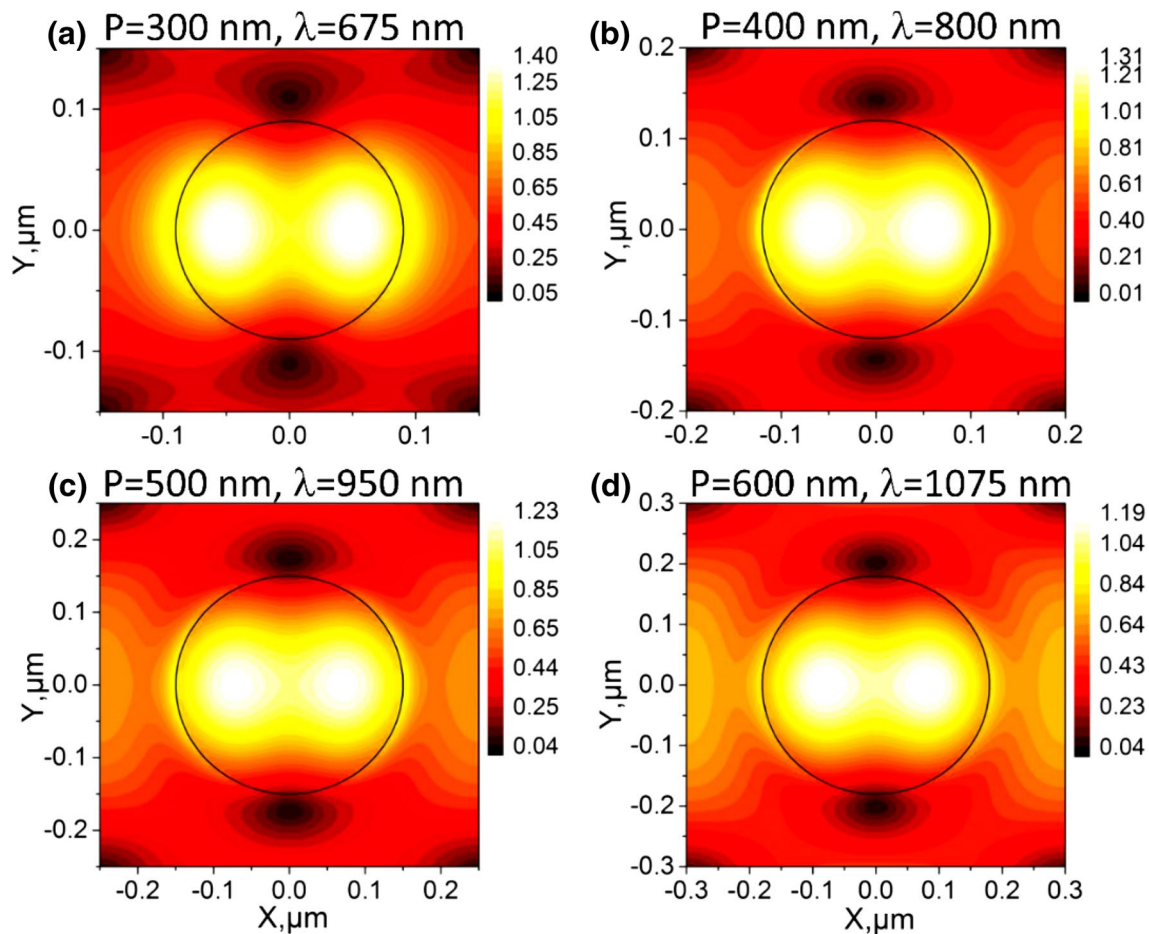


**Fig. 8** The E field distribution in the  $x$ - $y$  cross section near the bottom of a single nanopillar for wavelengths where zero reflectance appears with different  $P$

range of wavelengths. In order to demonstrate the antireflection capability of the SCS at different incident angles and polarization modes of light, the reflectance spectrum of Si with  $\text{TiO}_2/\text{SiO}_2$  double-layer ARCs for TM and TE polarized light were plotted as Fig. 9c and d, respectively. The reflectance of ARCs varies from 0 to 40% for TM polarized light and 0–60% for TE polarized light with incident angle ranging from  $0^\circ$  to  $60^\circ$ . In comparison, the reflectance of SCS remains less than 5% in wavelength range of 400–2200 nm with incident angle varying from  $0^\circ$  to  $40^\circ$  for TM polarized light, and the reflectance is less than 10% in nearly full spectrum over  $0^\circ$ – $50^\circ$ . For TE polarized light, the reflectance of SCS stays less than 5% for wavelength of 400–2200 nm and incident angle of  $0^\circ$ – $40^\circ$ , which is similar to the TM polarized light condition. The reflectance increases slightly in full spectrum as the angle of incidence increases, which is still much less than the reflectance of ARCs. Remarkably, for wavelengths of 300–1100 nm, the reflectance almost stays unchanged with incident angle varying from  $0^\circ$  to  $60^\circ$  for both TM

and TE polarized light. To sum up, the SCS possesses excellent omnidirectional antireflection properties in full spectrum with polarization insensitivity.

### 3.3 Experimental method

To support the result of simulation, the optimized SCS with the same parameters was fabricated and characterized. The SCS was fabricated on a  $3\text{ cm} \times 3\text{ cm}$ , 300- $\mu\text{m}$ -thick monocrystalline silicon wafer (p-type). The wafer was first cleaned in a 3:1 solution of  $\text{H}_2\text{SO}_4:\text{H}_2\text{O}_2$  for 60 min, rinsed with DI water. After that, as shown in Fig. 10, the ultrasonically dispersed solution of polystyrene spheres (PS) with the same diameter of 500 nm was injected onto the surface of DI water slowly by a syringe so as to form close-packed PS arrays by their self-assembling properties, and then the close-packed PS arrays were deposited on the cleaned silicon wafer by slowly lifting up.

The diameters of the PSs were then reduced after a reactive ion etching (RIE) process with  $\text{O}_2$  plasmas to

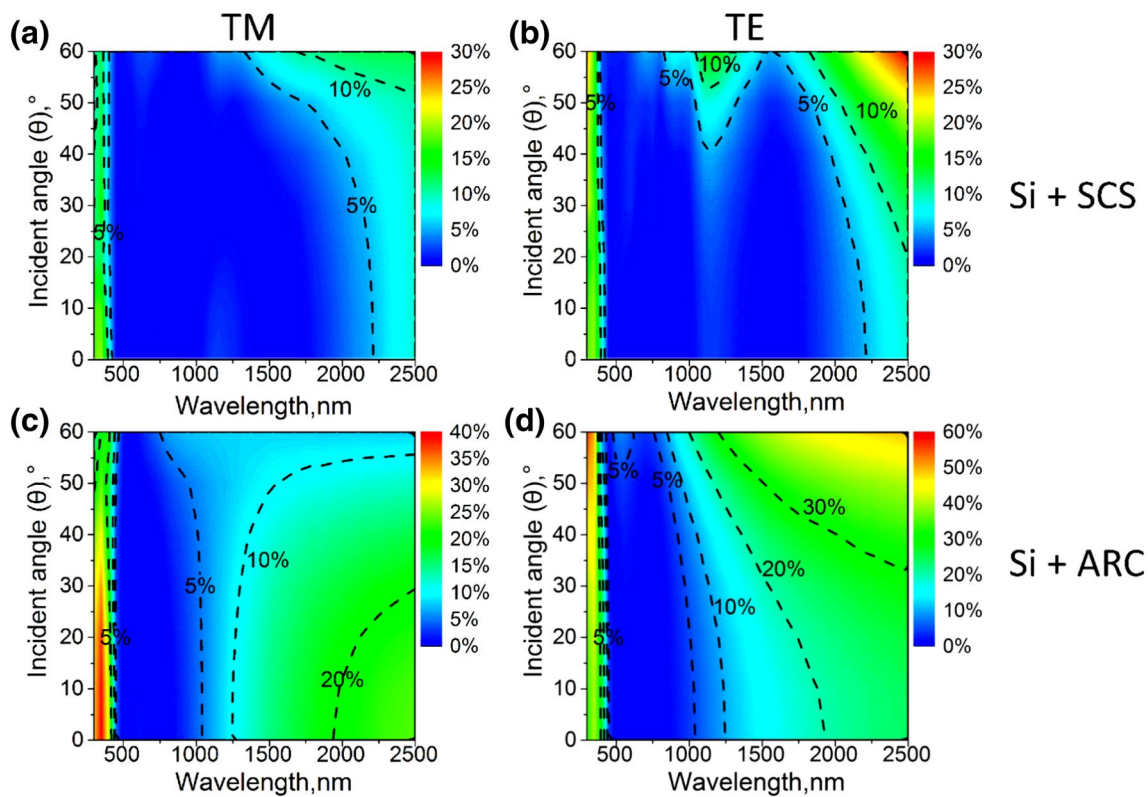
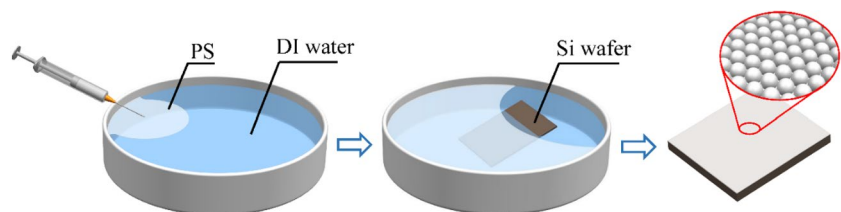


**Fig. 9** Simulative reflectance spectra of optimized SCS ( $H = 250$  nm,  $D = 300$  nm,  $P = 500$  nm,  $h_1 = 105$  nm and  $h_2 = 55$  nm) **a** with TM polarized light **b** with TE polarized light; **c**

Simulative reflectance spectra of the Si with  $\text{TiO}_2/\text{SiO}_2$  double-layer ARCs with TM polarized light **d** with TE polarized light

**Fig. 10** Procedure of depositing the closed-packed PS arrays on a silicon wafer surface



a diameter of 300 nm as shown in Fig. 11a. Afterwards, the nanopillars were formed by means of inductively coupled plasma (ICP) etching as shown in Fig. 11b. The PSs were then dissolved in chlorobenzene, leaving behind on the silicon wafer surface a nanopillars array as shown in Fig. 11c. Finally, the ARCs of  $\text{TiO}_2$  and  $\text{SiO}_2$  were deposited on the structured surface of the silicon wafer layer by layer with a magnetron sputtering procedure as shown in Fig. 11d and Fig. 10e respectively.

For characterization, the morphology of fabricated samples were observed by a field emission scanning electron microscopy (FESEM), and the reflectance/absorbance spectrum were obtained by the Agilent Cary-5000 UV-Vis-NIR spectrophotometer.

### 3.4 Experimental results

Figure 12 gives the multi-angle absorbance of the fabricated SCS with non-polarized light for wavelengths from 300 to 2500 nm. The inserted picture is the FESEM image with  $20^\circ$  tilted view of the fabricated SCS. The SCS on the 300- $\mu\text{m}$ -thick Si wafer obtains an ultra-high absorbance at wavelengths of 400–1000 nm for wide range of incident angles, especially achieving an average absorbance of  $\sim 96.7\%$  for incident angle  $\theta = 20^\circ$ . Moreover, the absorbance curves alter slightly as the angle of incidence changes from  $0^\circ$  to  $60^\circ$ , but the average absorbance remains higher than  $\sim 95.8\%$  for wavelengths of 400–1000 nm. This perfectly matches the simulation



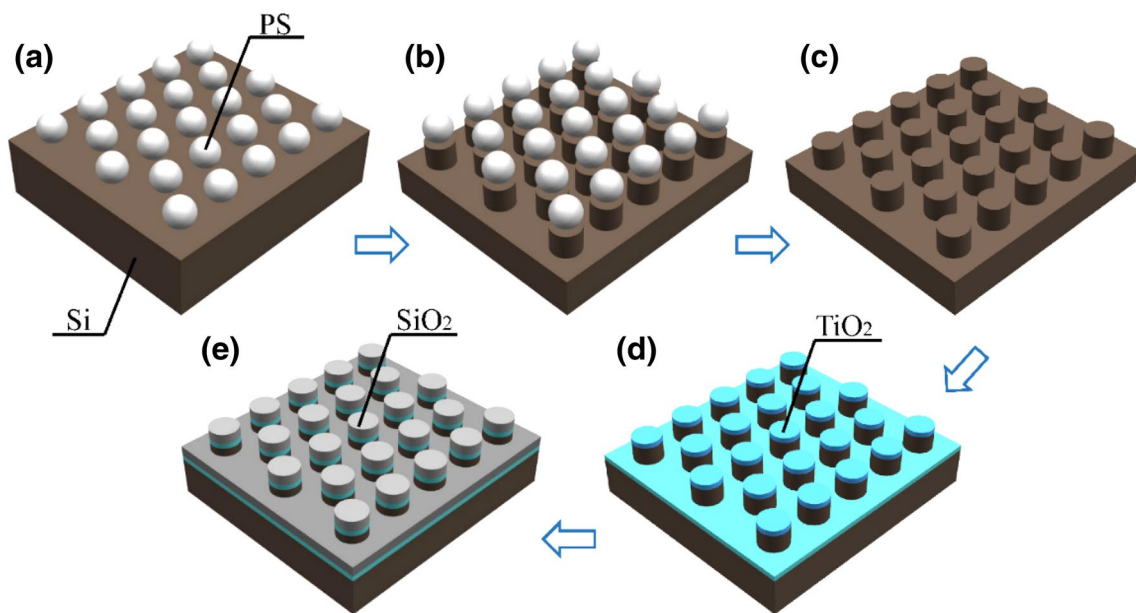


**Fig. 11** Diagram of the SCS forming procedure. **a** The diameters of the PSs were reduced after reactive ion etching (RIE); **b** the nanopillars were formed by means of ICP etching; **c** the PSs were dissolved

in chlorobenzene; **d, e** the ARCs of TiO<sub>2</sub> and SiO<sub>2</sub> were deposited by magnetron sputtering

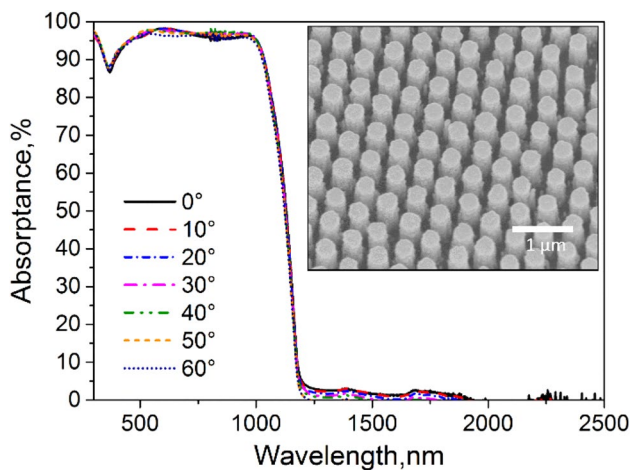


**Fig. 12** Multi-angle absorbance of the SCS with non-polarized light obtained by UV–Vis–NIR spectrophotometer. The inserted picture is the FESEM image with 20° tilted view of the fabricated SCS

results plotted in Fig. 11a and b of the excellent omnidirectional antireflection performance for wavelengths of 400–1000 nm with both TM and TE polarized light. On the contrary, the incident light for wavelengths greater than 1100 nm is barely absorbed due to the limit of the silicon’s bandgap. This part of light is assumed to be entirely utilized by other components of the PV-TE hybrid system in the simulation with a semi-infinite Si substrate. However, the smooth untreated back surface of a 300-μm-thick Si wafer would reflect a portion of unabsorbed light, as a

result, influence the measurement of antireflection abilities of the SCS on front surface. Therefore, for quantitative analyses of the difference between experimental and simulation results, the reflectance for wavelengths greater than 1100 nm is unnecessary to be involved.

Figure 13 shows the comparison of reflectance spectrum between simulation and experiment results at wavelengths from 300 nm to 1100 nm for incident angle of 30° and 60° with TM and TE polarized light, respectively. The experimental data agree well with the simulation results with wavelengths less than 1000 nm because the Si wafer is still not thick enough to absorb the light of 1100 nm wavelength. The differences of reflectance spectrum around 300 nm wavelength are mainly caused by the rough surface of the fabricated sample comparing to the ideal surface of simulation model. Further, the differences around 450 nm wavelength are attributed to the different refractive indexes between bulk material (for simulation) and the film (for experiment), which cause a slight disagreement to the double-layer ARCs matching conditions. Nevertheless, the average reflectance difference between simulation and experimental results for wavelengths of 300–1000 nm still maintain at low values of 1.66, 2.84, 1.51 and 1.39% corresponding to Fig. 13a–d respectively. To sum up, the SCS that we have designed in this work is applied to crystalline Si substrate, but the concept of the design method can be applied to other material for ultra-broadband spectrum regulation.

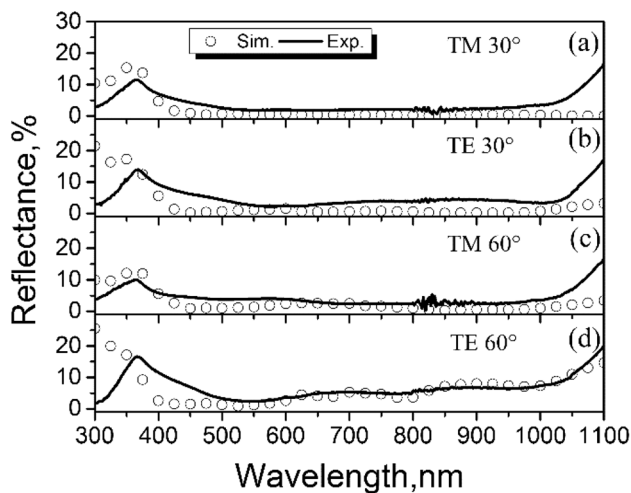


**Fig. 13** Comparison of reflectance spectrum between simulation and experiment results at wavelengths from 300 nm to 1100 nm for incident angle of 30° **a** with TM polarized light **b** with TE polarized light, and **c** for incident angle of 60° with TM polarized light **d** with TE polarized light

## 4 Conclusions

In conclusion, a subwavelength composite structure (SCS) has been proposed for full-spectrum omnidirectional antireflection, which is designed for a PV-TE hybrid system to enhance the utilization of solar energy. It consists of the periodic hexagonal array of silicon nanopillars and the misaligned stacked double-layer antireflection coatings (ARCs). After simulation researching by FDTD, it is found that the outstanding antireflection properties of the SCS are not only respectively due to the interference effect of the double-layer ARCs and the scattering effect of the nanopillars, but also due to the gradient refractive indexes in the air/Si interface and the waveguide resonances stimulated by nanopillars and surrounding materials, which are caused by the composition of nanopillars and double-layer ARCs. Afterwards, the SCS is fabricated by ICP etching and magnetron sputtering, and characterized by FESEM and UV-Vis-NIR spectrophotometer. The experimental results match well with the simulation results, which confirm the outstanding abilities for photons management of the SCS. Overall, this work paves the way to full-spectrum solar energy utilization suitable for the PV-TE hybrid system, and this antireflection concept can be applied to other materials for particular ultra-broadband spectrum regulation.

**Acknowledgements** This work was financially supported by the National Natural Science Foundation of China (Grant No. 51590901 and 51336003).

## References

1. L. Yang, Y. Xuan, *J. Quant. Spectrosc. Radiat. Transf.* **151**, 5–12 (2015)
2. Y. Liu, W. Zi, S.F. Liu, B. Yan, *Sol. Energy Mater. Sol. Cell* **140**, 180–186 (2015)
3. J.B. Kim, C.I. Yeo, Y.H. Lee, S. Ravindran, Y.T. Lee, *Nanoscale Res. Lett.* **9**, 54 (2014)
4. S. Chhajed, M.F. Schubert, J.K. Kim, E.F. Schubert, *Appl. Phys. Lett.* **93**, 251108 (2008)
5. X.H. Li, P.C. Li, D.Z. Hu, D.M. Schaadt, E.T. Yu, *J. Appl. Phys.* **114**, 44310 (2013)
6. K.M.A. Sobahan, Y.J. Park, J.J. Kim, C.K. Hwangbo, *Opt. Commun.* **284**, 873–876 (2011)
7. S. Tsai, H. Chang, H. Wang, S. Chen, C. Lin, S. Chen, Y. Chueh, J. He, *ACS Nano* **5**, 9501–9510 (2011)
8. P. Kuang, M. Hsieh, S. Lin, *J. Appl. Phys.* **117**, 215309 (2015)
9. J.W. Leem, Y.M. Song, Y.T. Lee, J.S. Yu, *Appl. Phys. B* **99**, 695–700 (2010)
10. Q. Yang, X.A. Zhang, A. Bagal, W. Guo, C.H. Chang, *Nanotechnology* **24**, 235202 (2013)
11. B. Liu, S. Qiu, N. Chen, G. Du, J. Sun, *Mater. Sci. Semicond. Process.* **16**, 1014–1021 (2013)
12. M.H. Elshorbagy, K. Abdel-Hady, H. Kamal, J. Alda, *Opt. Commun.* **390**, 130–136 (2017)
13. U. Sikder, M.A. Zaman, *Opt. Laser Technol.* **79**, 88–94 (2016)
14. B. Dudem, J.W. Leem, M. Choi, J.S. Yu, *Appl. Phys. B* **118**, 439–447 (2015)
15. R. Singh, M. Kumar, M. Saini, A. Singh, B. Satpati, T. Som, *Appl. Surf. Sci.* **418**, 225–231 (2017)
16. S. Sali, M. Boumaour, M. Kechouane, S. Kermadi, F. Aitamar, *Phys. B* **407**, 2626–2631 (2012)
17. S.K. Sardana, V.S.N. Chava, V.K. Komarala, *Appl. Surf. Sci.* **347**, 651–656 (2015)
18. P. Kuang, S. Eyderman, M. Hsieh, A. Post, S. John, S. Lin, *ACS Nano* **10**, 6116–6124 (2016)
19. P. Karadan, A.A. Anappara, V.H.S. Moorthy, C. Narayana, H.C. Barshilia, *RSC Adv* **6**, 109157–109167 (2016)
20. B.D. Park, J.W. Leem, J.S. Yu, *Appl. Phys. B* **105**, 335–342 (2011)
21. E. Garnett, P. Yang, *Nano Lett.* **10**, 1082–1087 (2010)
22. K. Park, H.J. Choi, C. Chang, R.E. Cohen, G.H. McKinley, G. Barbastathis, *ACS Nano* **6**, 3789–3799 (2012)
23. D.A. Zuev, O.A. Novodvorsky, E.V. Khaydukov, O.D. Khramova, A.A. Lotin, L.S. Parshina, V.V. Rocheva, V.Y. Panchenko, V.V. Dvorkin, A.Y. Poroykov, G.G. Untila, A.B. Chebotareva, T.N. Kost, M.A. Timofeyev, *Appl. Phys. B* **105**, 545–550 (2011)
24. J.W. Leem, Y.M. Song, Y.T. Lee, J.S. Yu, *Appl. Phys. B* **100**, 891–896 (2010)
25. Web site for NREL's AM1.5 Standard Dataset. <http://redc.nrel.gov/solar/spectra/am1.5>. Accessed 19 Jun 2017
26. D. Kraemer, L. Hu, A. Muto, X. Chen, G. Chen, M. Chiesa, *Appl. Phys. Lett.* **92**, 243503 (2008)
27. E.A. Chávez-Urbiola, Y.V. Vorobiev, L.P. Bulat, *Sol. Energy* **86**, 369–378 (2012)
28. M.L. Kuo, D.J. Poxson, Y.S. Kim, F.W. Mont, J.K. Kim, E.F. Schubert, S.Y. Lin, *Opt. Lett.* **33**, 2527–2529 (2008)
29. J.W. Leem, Y.M. Song, J.S. Yu, *Appl. Phys. B* **107**, 409–414 (2012)
30. Y. Zhang, Y. Xuan, *Sol. Energy Mater. Sol. C* **144**, 68–77 (2016)
31. Y. Xu, Y. Xuan, L. Yang, *Energy Convers. Manage.* **103**, 533–541 (2015)
32. S.A. Boden, D.M. Bagnall, *Appl. Phys. Lett.* **93**, 133108 (2008)
33. P. Spinelli, M.A. Verschuuren, A. Polman, *Nat. Commun.* **3**, 692 (2012)

34. H.A. Macleod, *Thin-Film Optical Filters* (Adam Hilger Ltd, Bristol, 1986)
35. E.D. Palik, *Handbook of Optical Constants of Solids*. J. Mod. Opt. **33**, 189 (1985)
36. J. Berenger, J. Comput. Phys. **127**, 363–379 (1996)
37. X. Meng, E. Drouard, G. Gomard, R. Peretti, A. Fave, C. Seassal, *Opt. Express* **20**(Suppl 5), A560–A571 (2012)
38. G. Grzela (ed.), *Directional Light Emission and Absorption by Semiconductor Nanowires* (Eindhoven University of Technology, Netherland, 2013)